

## Probability Distributions for the Inner Scale and the Refractive Index Structure Parameter and Their Implications for Flux Averaging

EDGAR L. ANDREAS

*U.S. Army Cold Regions Research and Engineering Laboratory, Hanover, New Hampshire*

CHRISTOPHER W. FAIRALL

*NOAA/Environmental Technology Laboratory, Boulder, Colorado*

P. OLA G. PERSSON

*Cooperative Institute for Research in Environmental Sciences, University of Colorado, Boulder, Colorado*

PETER S. GUEST

*Naval Postgraduate School, Monterey, California*

(Manuscript received 5 May 2002, in final form 6 January 2003)

### ABSTRACT

Defining the averaging time required for measuring meaningful turbulence statistics is a central problem in boundary layer meteorology. Path-averaging scintillation instruments are presumed to confer some time-averaging benefits when the objective is to measure surface fluxes, but that hypothesis has not been tested definitively. This study uses scintillometer measurements of the inner scale ( $l_0$ ) and the refractive index structure parameter ( $C_n^2$ ) to investigate this question of required averaging time. The first conclusion is that the beta probability distribution is useful for representing  $C_n^2$  and  $l_0$  measurements. Consequently, beta distributions are used to set confidence limits on  $C_n^2$  and  $l_0$  values obtained over various averaging periods. When the  $C_n^2$  and  $l_0$  time series are stationary, a short-term average of  $C_n^2$  or  $l_0$  can be as accurate as a long-term average. However, as with point measurements, when time series of path averaged  $C_n^2$  or  $l_0$  values are nonstationary, turbulent surface fluxes inferred from these  $C_n^2$  and  $l_0$  values can be variable and uncertain—problems that path averaging was presumed to mitigate. Because nonstationarity is a limiting condition, the last topic is quantifying the nonstationarity with a published nonstationarity ratio and also by simply counting zero crossings in the time series.

### 1. Introduction

The wide-ranging fields of atmospheric optics and boundary layer meteorology intersect when the subject is optical turbulence. The classic works by Tatarskii (1961, 1971) and Chernov (1967) define the scope of this intersection. In more recent work, Andreas (1990) assembled classic papers from both disciplines that focus on obtaining turbulent fluxes in the atmospheric boundary layer from propagation statistics obtained at optical or other electromagnetic (EM) wavelengths.

This idea of using the propagation statistics of EM waves—especially those that quantify scintillation—to infer turbulent properties of the atmospheric boundary

layer has been around for at least 30 yr (e.g., Strohbehn 1970; Gray and Waterman 1970; Gurvich et al. 1974). Because of the need to evaluate the surface energy budget over terrain that may be inhomogeneous, the emphasis in the last 15 yr has been on using scintillation to infer the surface fluxes of heat, moisture, and momentum (e.g., Kohsiek and Herben 1983; Hill et al. 1988, 1992a,b; Andreas 1989b, 1992; Thiermann and Grassl 1992; Green et al. 1994; De Bruin et al. 1995, 2002; Nieveen and Green 1999; Hartogensis et al. 2002).

Two propagation statistics are commonly used to estimate turbulent fluxes in the atmospheric surface layer: the refractive index structure parameter  $C_n^2$  and the inner scale of turbulence  $l_0$ . The refractive index structure parameter sets the level of the inertial-convective subrange for the one-dimensional refractive index spectrum  $\Phi_n$  (e.g., Andreas 1987):

$$\Phi_n(\kappa) = 0.249C_n^2\kappa^{-5/3}, \quad (1)$$

*Corresponding author address:* Dr. Edgar L. Andreas, U.S. Army Cold Regions Research and Engineering Laboratory, 72 Lyme Road, Hanover, NH 03755-1290.  
E-mail: eandreas@crrel.usace.army.mil

where  $\kappa$  is the magnitude of the turbulence wavenumber. The refractive index spectrum in the inertial–convective subrange, however, can also be expressed in more familiar meteorological variables:

$$\Phi_n(\kappa) = \beta_n N_n \varepsilon^{-1/3} \kappa^{-5/3}, \quad (2)$$

where  $N_n$  is the dissipation rate of the variance in refractive index,  $\varepsilon$  is the dissipation rate of turbulent kinetic energy, and  $\beta_n$  ( $\sim 0.4$ ; Andreas 1987) is the Kolmogorov (or Corrsin) constant for the refractive index spectrum.

For the optical wavelengths that we use,  $C_n^2$  relates directly to the temperature structure parameter  $C_T^2$  through

$$C_n^2 = A^2(\lambda, P, T, Q) C_T^2. \quad (3)$$

Here,  $A$  is a known function of the EM wavelength ( $\lambda$ ) and the average barometric pressure ( $P$ ), temperature ( $T$ ), and specific humidity ( $Q$ ) (e.g., Andreas 1988b).

In (3), we ignore contributions from the humidity and temperature–humidity structure parameters, which are usually negligible unless the absolute value of the Bowen ratio is small (e.g., Wesely and Alcaez 1973; Wesely 1976; Thiermann and Grassl 1992; Hill et al. 1992b). Over sea ice, where we made our measurements, the magnitude of the Bowen ratio is almost always large enough for (3) to be a good approximation (Andreas and Cash 1996).

Because the temperature spectrum also obeys equations like (1) and (2), we can rewrite (3) as

$$C_n^2 = A^2(\beta_T/0.249) N_T \varepsilon^{-1/3}, \quad (4)$$

where  $\beta_T$  is the Kolmogorov constant for the temperature spectrum, and  $N_T$  is the dissipation rate of temperature variance. As a result,  $C_n^2$  is related to dissipation rates that are commonly used in the inertial–dissipation method for flux estimation (e.g., Fairall and Larsen 1986).

The inner scale  $l_0$  likewise relates to features of the refractive index spectrum;  $l_0$  is approximately the turbulent eddy size that separates the inertial–convective subrange from the dissipation region and is roughly 7 times as large as the Kolmogorov microscale. Because at optical wavelengths the temperature spectrum and the refractive index spectrum have identical shapes at large wavenumbers, we can write (Hill and Clifford 1978)

$$l_0 = [9\Gamma(1/3)\beta_T D]^{3/4} \varepsilon^{-1/4}, \quad (5)$$

where  $\Gamma$  is the gamma function and  $D$  is the thermal diffusivity of air. Like  $C_n^2$ ,  $l_0$  is related to a dissipation value (i.e.,  $\varepsilon$ ) that is required for using the inertial–dissipation method to estimate the turbulent surface fluxes.

The preferred method for estimating the surface stress (or momentum flux) and the sensible heat flux from these scintillation measurements uses similarity relations for the dissipation rate  $\varepsilon$  and for the temperature structure parameter. The two relevant equations are

(e.g., Andreas 1988b; Thiermann and Grassl 1992; Hill 1997)

$$t_* = \left[ \frac{z^{2/3} C_n^2}{A^2 g(\zeta)} \right]^{1/2} \quad \text{and} \quad (6)$$

$$u_* = \left[ \frac{\varepsilon k z}{\phi_\varepsilon(\zeta)} \right]^{1/3}. \quad (7)$$

Here,  $z$  is the path height,  $k$  is the von Kármán constant, and  $g(\zeta)$  and  $\phi_\varepsilon(\zeta)$  are semiempirical Monin–Obukhov similarity functions of the stability parameter  $\zeta = z/L$ , where  $L$  is the Obukhov length (see the appendix). Also in these,  $u_*$  is the friction velocity and  $t_*$  is a temperature flux scale such that  $\tau = \rho u_*^2$  is the surface stress and  $H_s = -\rho c_p u_* t_*$  is the surface sensible heat flux, where  $\rho$  is the air density and  $c_p$  is the specific heat of air at constant pressure. Note that, because of the square root, (6) is ambiguous as to the sign of  $t_*$ ; we must evaluate this by other means.

Using scintillation to estimate the turbulent surface fluxes is attractive because the EM waves propagate over a finite path. The propagation statistics are thus path averaged, as would be any turbulence quantity derived from them. Presumably, such path averaging mitigates the effects of minor nonstationarity or surface heterogeneity that often confound turbulence measurements made with point sensors.

A second supposed benefit of using EM propagation measurements of  $C_n^2$  and  $l_0$  to determine  $u_*$  and  $t_*$  is that statistically reliable values of  $C_n^2$  and  $l_0$  can be obtained with very short averaging times, on the order of 1 min or less (Wyngaard and Clifford 1978; Frehlich 1988, 1992). By extension, this result would seem to suggest that  $\tau$  and  $H_s$  could also be measured using path-averaging instruments with much shorter averaging times than the 30–60 min of averaging typically required for point measurements (Haugen et al. 1971; Wyngaard 1973; Sreenivasan et al. 1978).

The rationale for this idea that short flux-averaging times are possible is that a path-averaging sensor samples many more turbulent eddies per unit time than a point sensor (Andreas 1988a). Some of those eddies would, presumably, be the larger ones that manifest as nonstationarity in a time series of point measurements. The path averaging supposedly would smooth out the effects of these large eddies and thereby reduce the sampling error common in point measurements of turbulent fluxes.

Even if this scenario is accurate, though, we are still skeptical that path-averaged scintillation statistics can routinely yield meaningful estimates of  $\tau$  and  $H_s$  for averaging times on the order of minutes. Obtaining these turbulent flux estimates requires convolving the scintillation statistics  $C_n^2$  and  $l_0$  (or, equivalently,  $\varepsilon$ ) iteratively with the Monin–Obukhov similarity functions  $g(\zeta)$  and  $\phi_\varepsilon(\zeta)$  in (6) and (7). All evaluations of these similarity functions that we know of, however, are based

on point measurements of mean meteorological and turbulence quantities averaged for 30–60 min (e.g., Businger et al. 1971; Dyer and Bradley 1982; Höögström 1988; Oncley et al. 1996; Edson and Fairall 1998). It is not obvious to us that, in general, combining minute averages of  $C_n^2$  and  $l_0$  with functions based on at least 30-min averages yields meaningful values of  $\tau$  and  $H_s$  (cf. Andreas 1988a). If short-term averages of  $C_n^2$  and  $l_0$  are representative of time series averaged for, say, 30–60 min, however, using these short-term averages in (6) and (7) to estimate  $\tau$  and  $H_s$  may be defensible.

Here we address these issues of how to properly average scintillation-derived values of  $C_n^2$  and  $l_0$  for the purpose of estimating the turbulent surface fluxes. First we review the time-averaging constraints for evaluating Monin–Obukhov similarity functions to highlight our concern over combining similarity functions and short-term scintillometer averages. Next we show samples of histograms for  $C_n^2$  and  $l_0$  values selected from 600 h of scintillometer data collected during the experiment to study the Surface Heat Budget of the Arctic Ocean (SHEBA). We find that beta probability distributions fit both variables well. Using these beta distributions, we then compute error bars for several representative hour-long time series of SHEBA  $C_n^2$  and  $l_0$  values. This error analysis reveals that nonstationarity can have pronounced effects on these path-averaged  $C_n^2$  and  $l_0$  values, contrary to some of our earlier speculation. As a result, we conclude that short-term averages of  $C_n^2$  and  $l_0$  can yield reliable short-term averages of  $\tau$  and  $H_s$  only for quasi-stationary time series.

## 2. Observations

SHEBA was a multidisciplinary, yearlong experiment on drifting sea ice in the Beaufort Gyre (Uttal et al. 2002). Andreas et al. (1999) and Persson et al. (2002) describe our SHEBA program. Andreas et al. (1999) show a picture of the scintillometer we used to obtain the data reported here, and Andreas et al. (2000) give a preliminary report of our current analysis.

Our SHEBA scintillometer was an SLS20 system made by Scintec Atmosphärenmesstechnik GmbH of Tübingen, Germany (Thiermann 1992). Its source is a laser of 0.685- $\mu\text{m}$  wavelength. We operated this system over a 350-m path at a height of 2.88 m for our 1997 SHEBA measurements and over a 300-m path at a height of 2.60 m for our 1998 measurements. The surface was generally snow-covered sea ice.

The fundamental data that the SLS20 reports are minute averages of  $C_n^2$  and  $l_0$ . To fairly compare the 1997 and 1998 datasets, we extrapolated both the  $C_n^2$  and  $l_0$  values from the two sets to a common height of 3 m on the basis of (5), (6), and (7) by ignoring the small effects of stability on the extrapolation (Andreas et al. 2000).

De Bruin et al. (2002) and Hartogensis et al. (2002) raise issues about some apparent biases in values of  $u_*$

and  $H_s$  derived from SLS20 measurements. De Bruin et al. speculate that these biases may result from a small signal-to-noise ratio or from the effects of inactive turbulence. Hartogensis et al. reduce these biases by assuming that the separation between the split beams at the laser's source is 2.6 mm instead of the 2.7 mm that the manufacturer claims.

While we cannot rule out the possibility that similar biases affect our SLS20 measurements, their effects are secondary to our theme here. Hartogensis et al. (2002) demonstrate that SLS20 measurements of  $\varepsilon$  and  $C_n^2$  are correlated with measurements of these same quantities made with small, fast-responding point instruments. That is, the scintillometer is responding to  $l_0$  and  $C_n^2$ , and that property makes it adequate for our purpose. We are not here to prove that scintillometers can measure  $u_*$  and  $H_s$  accurately but rather to consider the more fundamental question of how to average scintillometer data to obtain these values.

Figure 1 shows a daylong time series of minute-averaged  $C_n^2$  and  $l_0$  values. Generally,  $l_0$  is inversely related to the wind speed; higher wind speeds increase the dissipation rate of turbulent kinetic energy, which, in turn, is associated with smaller  $l_0$  values [see (5)]. The behavior of  $C_n^2$  is not as easy to understand. On the one hand, higher wind speeds usually foster mixing, which erodes any vertical temperature gradient, and so  $C_n^2$  decreases (cf. Frederickson et al. 2000). On the other hand, if some process, such as radiative heating or cooling, can maintain a vertical temperature gradient, a higher wind speed would increase the magnitude of the sensible heat flux and, thereby, increase  $C_n^2$ .

Later we will compute statistics from series of  $C_n^2$  and  $l_0$ , such as in Fig. 1, and derive confidence limits from these statistics. Such analyses get complicated if adjacent samples in the time series are correlated. The autocorrelation function quantifies the decorrelation time of a random process; the integral of the autocorrelation function over all time lags defines the interscale  $\mathfrak{S}$  (e.g., Lumley and Panofsky 1964, p. 36ff) that represents this decorrelation time. Sample values separated in time by intervals of  $\mathfrak{S}$  or longer are essentially uncorrelated or independent.

As an estimate for the integral scale in the neutrally stratified atmospheric surface layer, Wyngaard (1973) uses  $\mathfrak{S} \sim z/U$ . Sreenivasan et al. (1978) build on Wyngaard's analysis and, from high-frequency time series of temperature, humidity, and velocity components, compute autocorrelation functions. From these autocorrelation functions, they deduce

$$\mathfrak{S} = \frac{4z}{U}. \quad (8)$$

We use (8) to estimate the integral scale in our scintillometer data. Our scintillometer operated at heights a bit under 3 m; in (8), we, thus, use 3 m for  $z$ . The integral scale clearly increases as the wind speed de-

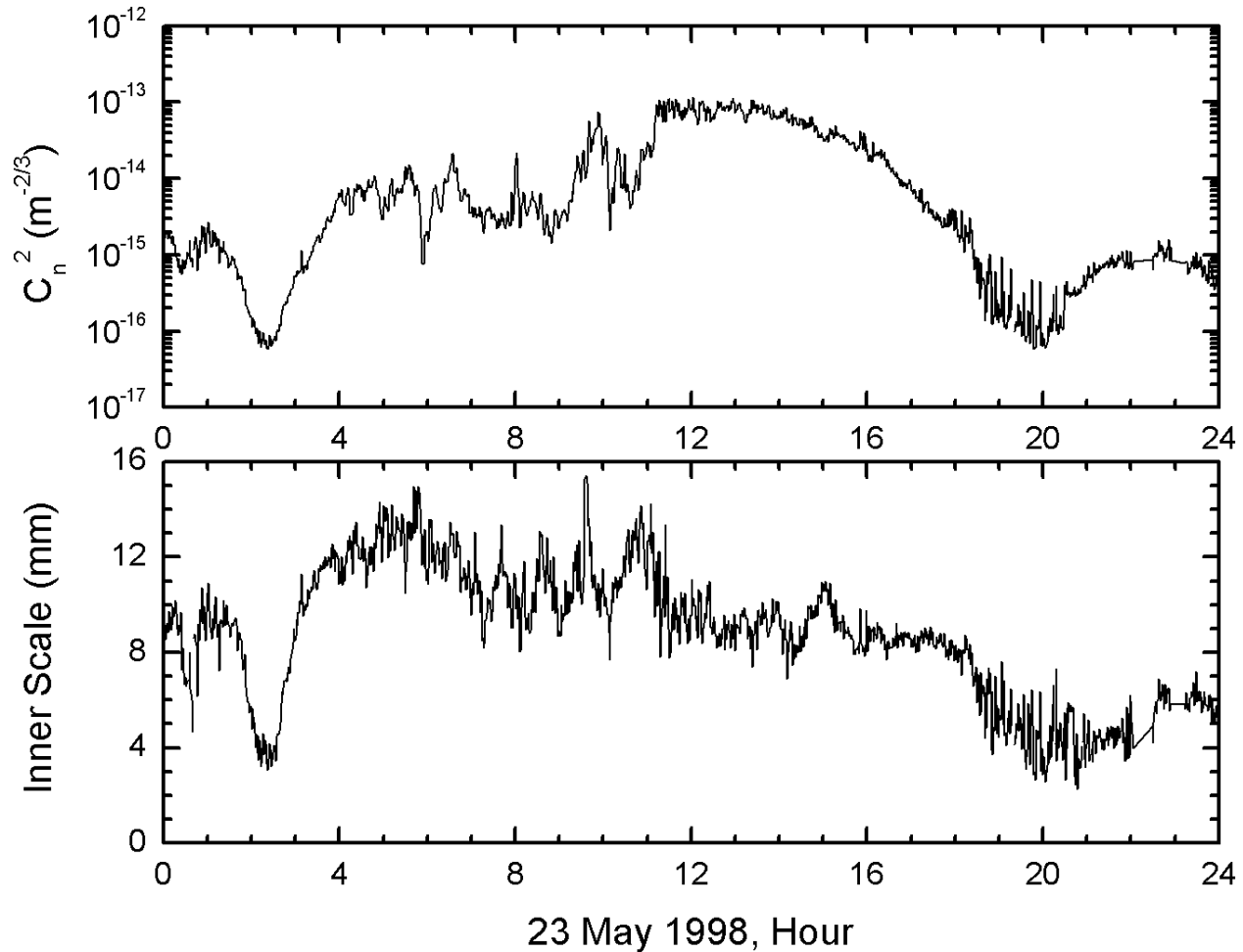


FIG. 1. A day of 1-min-averaged (bottom) inner scale ( $l_0$ ) and (top) refractive index structure parameter ( $C_n^2$ ) values at a height of 3 m from SHEBA.

creases; hence, the longest decorrelation time is associated with the lightest winds. In fewer than 10 of the 600 h of scintillometer data that survived our quality controls was the average hourly wind speed less than  $1 \text{ m s}^{-1}$ . Substituting  $1 \text{ m s}^{-1}$  and  $z = 3 \text{ m}$  in (8) gives 12 s as a conservative estimate for the decorrelation time of our raw scintillometer data. For most of the data, the decorrelation time is much shorter because the wind speed was higher. Because the only scintillometer data we use in our subsequent analyses are minute averages, we can be confident that these minute-averaged  $C_n^2$  and  $l_0$  values are independent. We thus need not worry about the complicating effects of correlated data in our statistical analysis.

### 3. Averaging to establish Monin–Obukhov similarity theory

Equations (6) and (7) are derived from Monin–Obukhov similarity theory. Evaluating the similarity functions  $g(\zeta)$  and  $\phi_\epsilon(\zeta)$  that make (6) and (7) work requires

measuring both means and covariances. In particular, we must measure the mean wind speed ( $U$ ) and temperature ( $T$ ) profiles and the covariances  $\overline{uw}$  ( $= -u_*^2$ ) and  $\overline{wT}$  ( $= -u_* t_*$ ), where the overbar denotes averaging. To have confidence in the resulting similarity functions, we must have confidence in the statistical properties of these averages. That is, we must average long enough to ensure reliable statistics.

Lumley and Panofsky (1964, p. 35ff), Wyngaard (1973), Sreenivasan et al. (1978), Andreas (1988a), and Lenschow et al. (1994), among others, estimate how long is long enough to average. Here we rely on the analyses by Wyngaard and Sreenivasan et al.

Building on work by Lumley and Panofsky (1964), Wyngaard (1973) estimates the averaging time  $T_x$  required to reduce the error in a measured mean  $\bar{x}$  to  $\delta_x \bar{x}$  as

$$T_x = 2\mathfrak{S}_x \frac{\overline{x^2}}{\delta_x^2 \bar{x}^2}, \tag{9}$$

where  $\mathfrak{S}_x$  denotes the integral scale of variable  $x$ , and

$\overline{x^2}$  is the ensemble variance about  $\bar{x}$ . Sreenivasan et al. (1978) evaluate  $\mathfrak{S}_x$  for quantities like  $U$ ,  $T$ ,  $\overline{uw}$ , and  $\overline{wt}$ . In general, they find

$$\mathfrak{S}_x = \frac{\alpha_x z}{U}, \quad (10)$$

where  $\alpha_x$  is 3.9, 4.9, 1.2, and 1.2 for  $U$ ,  $T$ ,  $\overline{uw}$ , and  $\overline{wt}$ , respectively.

Evaluating the Monin–Obukhov similarity functions requires measuring the vertical gradients in wind speed and potential temperature. We must, thus, require an accuracy in individual wind speed and temperature measurements of, say,  $5 \text{ cm s}^{-1}$  and  $0.1 \text{ K}$ , respectively. For a  $5 \text{ m s}^{-1}$  wind speed, this makes  $\delta_U = 0.01$ ; for an average temperature of  $293 \text{ K}$ ,  $\delta_T = 0.00034$ .

To estimate the averaging time for finding the vertical gradient in wind speed, we combine (9) and (10) to get

$$T_U = 2 \times 10^4 \left( \frac{3.9z}{U} \right) \left( \frac{\sigma_U^2}{U^2} \right), \quad (11)$$

where  $\sigma_U^2$  is the variance in the longitudinal component of the wind vector. Typically,  $\sigma_U/U \approx 0.1$  (e.g., Arya 1988). Hence, for a 10-m profiling tower in a  $5 \text{ m s}^{-1}$  wind,  $T_U \approx 1600 \text{ s} \approx 26 \text{ min}$  is an approximate averaging time.

Similarly, to measure the mean vertical temperature gradient, we must average according to

$$T_T = 1.7 \times 10^7 \left( \frac{4.9z}{U} \right) \left( \frac{\sigma_T^2}{T^2} \right). \quad (12)$$

When the sensible heat flux is on the order of  $100 \text{ W m}^{-2}$ ,  $\sigma_T^2$  is about  $0.5 \text{ K}^2$ . Hence, for an average temperature of  $293 \text{ K}$  and the other conditions as above,  $T_T \approx 970 \text{ s} \approx 16 \text{ min}$  is an approximate averaging time.

That is, measuring the mean profiles necessary to determine the Monin–Obukhov similarity functions requires averaging for 15–30 min.

To estimate the flux-averaging time, Wyngaard (1973) and Sreenivasan et al. (1978) write (9) as

$$T_{wx} = \frac{2\alpha_{wx}z}{\delta_{wx}^2 U} \left[ \frac{\overline{(wx)^2} - \overline{wx}^2}{\overline{wx}^2} \right], \quad (13)$$

where  $x$  is now the fluctuation in either the longitudinal velocity ( $u$ ) or temperature ( $t$ ). From Kansas data, Wyngaard estimates the bracketed quantity in (13) to be about 10 for both  $\overline{uw}$  and  $\overline{wt}$  for near-neutral stratification. Sreenivasan et al. report that this quantity is 15 and 32, respectively, for  $\overline{uw}$  and  $\overline{wt}$ .

An error of 10% (i.e.,  $\delta_{wx} = 0.1$ ) is about the best that has been demonstrated for eddy correlation measurements of the turbulent surface fluxes. Thus, for a measurement height of  $5 \text{ m}$ , a mean wind speed of  $5 \text{ m s}^{-1}$ , and with  $\alpha_{wx} = 1.2$  from Sreenivasan et al. (1978) for both  $\overline{uw}$  and  $\overline{wt}$ , (13) gives  $T_{uw} = T_{wt} \approx 40 \text{ min}$  when we use Wyngaard's (1973) value for the bracketed term in (13). When

we use the estimates for this term from Sreenivasan et al.,  $T_{uw} \approx 60 \text{ min}$  and  $T_{wt} \approx 128 \text{ min}$ .

In summary, using eddy correlation to measure the momentum and heat fluxes to within 10% for evaluating the Monin–Obukhov similarity functions requires roughly 1 h of averaging. (Admittedly, we have ignored stratification effects on these estimates for simplicity and because these effects are not well known for the required covariance statistics.) We could, of course, average the fluxes over shorter intervals to match the averaging time of about 15 min we estimated for the wind speed and temperature gradients. However, errors in the fluxes would increase with shorter averaging. From (13) we can estimate by how much. For example, reducing the averaging time from 1 h to 15 min would increase the flux error by a factor of 2—from 10% to 20% in our analysis.

We provide this review to establish the averaging constraints under which typical Monin–Obukhov similarity functions must be evaluated. Statistical theory and experiment suggest that evaluating these functions from only 15 min of averaging may be possible, but the results will be quite scattered (cf. Haugen et al. 1971; Wyngaard 1973, p. 141), especially because  $\zeta$  includes both  $u_*$  and  $t_*$  and their uncertainties are additive [see (A3)]. In fact, we know of no attempts to validate Monin–Obukhov similarity theory with such short averages. Almost all published similarity functions are based on averages of 30–60 min.

The hope is that scintillometer measurements, because of their path averaging, might provide relief from these averaging constraints. However, the reality is that computing surface fluxes from scintillation measurements requires using similarity functions derived from long averaging times. No evidence exists that Monin–Obukhov similarity theory is also valid for the 1–10-min fluxes often computed from scintillation data (e.g., Theirmann and Grassl 1992; De Bruin et al. 2002; Hartogensis et al. 2002). To us, assuming that Monin–Obukhov similarity functions derived from 30–60 min averages are equally valid when applied to short averages is unjustified.

If, however, the path averaging in scintillation measurements provides such a large, fast sample that, say, 10 min of averaging yields the same information that 30–60 min of averaging would, using existing Monin–Obukhov similarity functions for computing scintillometer-derived fluxes may be justified. In this paper, we thus study whether short-term samples of scintillometer  $C_n^2$  and  $l_0$  values faithfully represent the behavior of these quantities over 1 h. If the answer is “yes” in general, using short scintillometer averages and the Monin–Obukhov similarity functions to compute short-term fluxes is defensible because the path averaging has mitigated the time-averaging constraints that hamper point measurements. If the answer is “no,” however, scintillometers confer no time-averaging benefits because their data must still pass through the traditional

Monin–Obukhov similarity functions to yield surface fluxes.

**4.  $C_n^2$  and  $l_0$  distributions**

On using measurements of  $u_*$  and  $H_s$  from another Arctic experiment, the Arctic Ice Dynamics Joint Experiment (AIDJEX), Andreas (1989a) inferred  $C_n^2$  from a relation similar to (6) and found that a beta distribution fitted seasonal histograms of these values well. Andreas et al. (2000) show similar seasonal histograms of our SHEBA  $C_n^2$  and  $l_0$  measurements.

Briefly, a beta distribution requires four parameters: the mean  $\bar{x}$  and sample standard deviation  $s_x$  of the data and lower ( $a$ ) and upper ( $b$ ) limits beyond which the distribution is zero. Harr (1987, p. 79ff) or Andreas (1989a) provide more details on computing the beta probability distribution.

While seasonal histograms of the AIDJEX and SHEBA data establish the versatility of the beta distribution in representing  $C_n^2$  and  $l_0$  distributions, seasonal statistics are not really our interest here. Instead, we necessarily concentrate on the short-term behavior of  $C_n^2$  and  $l_0$  and find the beta distribution equally useful.

Figures 2–4 show histograms and beta distributions fitted to only 1 h (i.e., sixty 1-min averages) of  $C_n^2$  and  $l_0$  values for three different occasions. Because  $C_n^2$  can range over several orders of magnitude (see Fig. 1), we base calculations of the averages and standard deviations used for fitting these  $C_n^2$  histograms on  $\ln(C_n^2)$  rather than on  $C_n^2$ . Later, we will base statistical analyses of these three periods on beta distributions. Therefore, we present Figs. 2–4 to emphasize that beta distributions can fit both broad and narrow histograms comprising far fewer data points than in the seasonal histograms in Andreas (1989a) or Andreas et al. (2000).

Although the beta distribution requires four parameters (i.e.,  $\bar{x}$ ,  $s_x$ ,  $a$ ,  $b$ ), rather than the two needed for a normal distribution, for example, the fit is not especially sensitive to  $a$  and  $b$ . In the three  $C_n^2$  histograms in Figs. 2–4 and for the seasonal histograms in Andreas (1989a) and Andreas et al. (2000), we used the same  $a$  and  $b$  values,  $\ln(10^{-18})$  and  $\ln(10^{-12})$ , respectively. Likewise, for the three  $l_0$  histograms here, and for the seasonal histograms in Andreas et al. (2000), we used the same limits, 0 and 20 mm. We conclude that the beta distribution is a useful tool for representing broad or narrow histograms that result from few or many data samples. For our Arctic scintillometer data, the fit is fairly insensitive to the choices of  $a$  and  $b$ .

Although we have no theoretical justification for choosing the beta distribution, Harr (1987, p. 77ff) provides ample practical justification. Briefly, the beta distribution can be symmetric or skewed; it can approximate a normal or a lognormal distribution, where the latter is commonly used to model propagation statistics (e.g., Ben-Yosef and Goldner 1988; Frehlich 1992; Hill

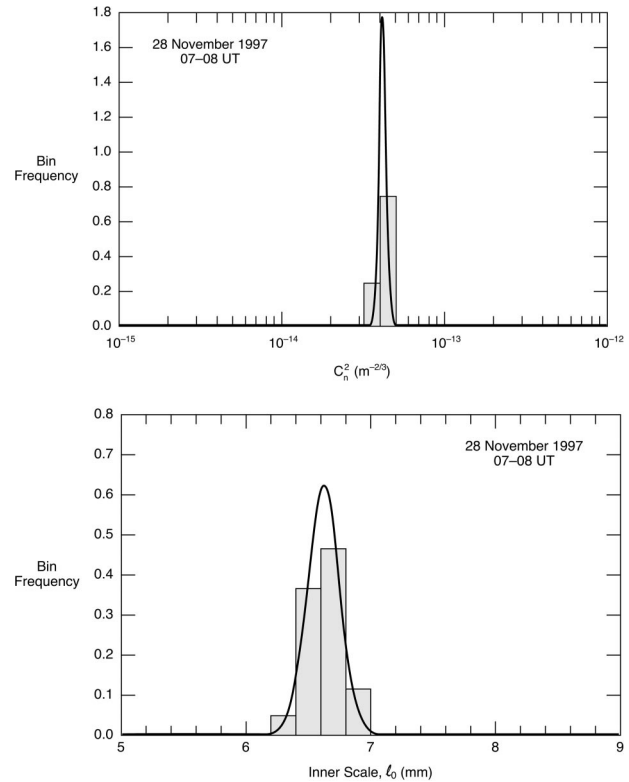


FIG. 2. Histograms of sixty 1-min-averaged (top)  $C_n^2$  and (bottom)  $l_0$  values measured at SHEBA between 0700 and 0800 UTC 28 Nov 1997. The solid line is the beta distribution fitted to the histogram. In the  $C_n^2$  plot, the lower and upper limits of the beta distribution,  $a$  and  $b$ , are  $\ln(10^{-18} \text{ m}^{-2/3})$  and  $\ln(10^{-12} \text{ m}^{-2/3})$ , respectively; in the  $l_0$  plot, these limits are 0 and 20 mm.

and Frehlich 1997). It can even represent a “bathtub” distribution.

Despite the constant lower and upper limits we impose on the  $C_n^2$  and  $l_0$  values in Figs. 2–4, the beta distribution is able to reproduce both wide (e.g., Fig. 4) and narrow (e.g., Figs. 2 and 3)  $C_n^2$  and  $l_0$  histograms. This ability of the beta distribution with fixed lower and upper limits to capture the features of the histogram, even when there are few points, is important for our later analysis.

Another important feature for our application is that the beta distribution is bounded by  $a$  and  $b$ . Some  $l_0$  histograms that we have plotted (e.g., Andreas et al. 2000) look bell shaped; we could have tried fitting these with a normal distribution. On occasion, however, the normal distribution would have predicted a finite probability that  $l_0$  could be negative—a physical impossibility. By using a beta distribution for  $l_0$  and setting the  $a$  value to 0, we prevent this unphysical result.

**5. Averaging  $C_n^2$  and  $l_0$**

With the knowledge that beta distributions can reliably represent distributions of  $C_n^2$  and  $l_0$ , we can set confidence intervals for measurements of  $C_n^2$  and  $l_0$ . In

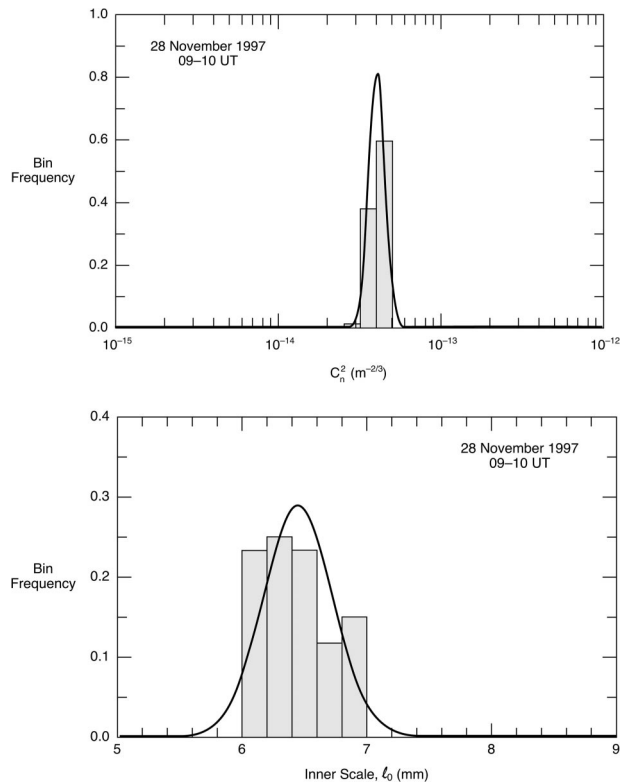


FIG. 3. As in Fig. 2, except these data are for 0900–1000 UTC 28 Nov 1997.

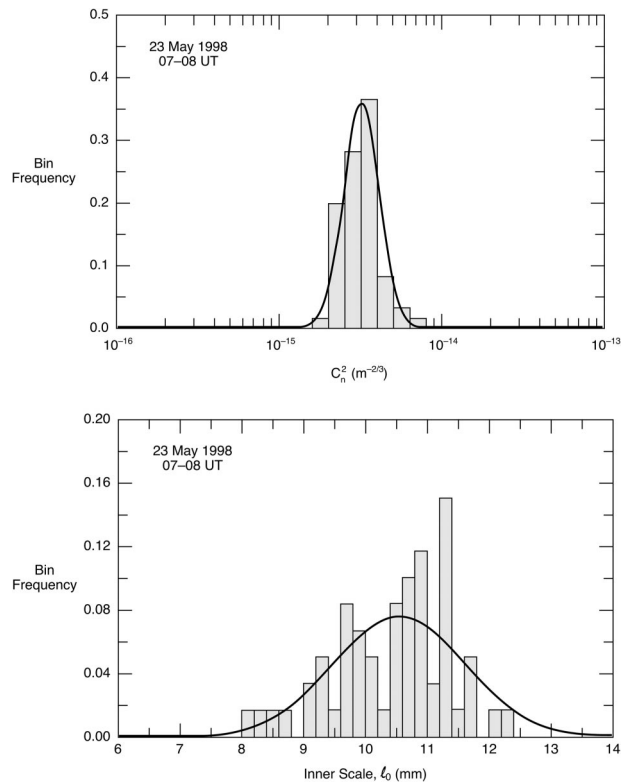


FIG. 4. As in Fig. 2, except these data are for 0700–0800 UTC 23 May 1998.

other words, we can investigate the role of averaging time in determining the confidence we have in various averages of  $C_n^2$  and  $l_0$ . Remember, the fundamental question we are researching is whether short-term averages of  $C_n^2$  and  $l_0$  can yield meaningful estimates of  $u_*$  and  $H_s$ . Our view, again, is that, because of the need to use empirical similarity functions to compute these fluxes, the answer is “yes” only when the short-term measurements of  $C_n^2$  and  $l_0$  faithfully represent the behavior of the  $C_n^2$  and  $l_0$  time series over 30–60 min.

Define a time-dependent average  $X(t)$  and standard deviation  $s(t)$  as

$$X(t) = \frac{1}{N} \sum_{i=1}^N x_i \quad \text{and} \quad (14)$$

$$s^2(t) = \frac{1}{N-1} \left[ \sum_{i=1}^N x_i^2 - NX^2(t) \right]. \quad (15)$$

Here  $x_i$  is the time series of minute averages of either  $C_n^2$  or  $l_0$ ,  $t = (N-1)\Delta t$ , and  $\Delta t$  is 1 min for our data. That is,  $X(t)$  and  $s(t)$  are the sample mean and sample standard deviation for all data in a time series from the first point to the  $N$ th point, which corresponds to time  $t$ .

Figure 2 shows histograms for the  $C_n^2$  and  $l_0$  values collected between 0700 and 0800 UTC 28 November 1997. Figure 5 shows the hour-long time series of these minute-averaged  $C_n^2$  and  $l_0$  values. The figure also in-

cludes the averages  $C_n^2(t)$  and  $l_0(t)$  computed with (14) between time zero and time  $t$  and 90% confidence intervals on the  $C_n^2$  and  $l_0$  populations at each minute based on beta distributions computed from the average  $[X(t)]$  and the standard deviation  $[s(t)]$  of each variable at time  $t$ . [As before, for  $C_n^2$ , all statistics are based on  $\ln(C_n^2)$ .] The lower and upper limits of the beta distribution for  $C_n^2$  here again correspond to  $10^{-18}$  and  $10^{-12} \text{ m}^{-2/3}$ ; for  $l_0$ , the limits are 0 and 20 mm.

In Fig. 5, we show 90% confidence intervals for the  $C_n^2$  and  $l_0$  populations (as opposed to confidence intervals on the respective means) because these intervals represent the variability in the path-averaged atmosphere as observed by the scintillometer. These intervals also show how effective path-averaging instruments are in smoothing out nonstationarity in the atmosphere.

Both the  $C_n^2$  and  $l_0$  time series in Fig. 5 support the contention that statistically meaningful values of these quantities can be obtained quite quickly. Here, after only 10 min of averaging, the 90% confidence intervals for both the  $C_n^2$  and  $l_0$  populations bracket the respective averages for the remainder of the hour and also bracket almost all of the subsequent minute-averaged values. That is, the first 10 min of data faithfully represent all the  $C_n^2$  and  $l_0$  values observed during the hour. For such series, using short-term averages of  $C_n^2$  and  $l_0$ —say 10-min averages—to make inertial-dissipation estimates of  $u_*$  and  $H_s$  seems reasonable. Averaging  $C_n^2$  and  $l_0$  for

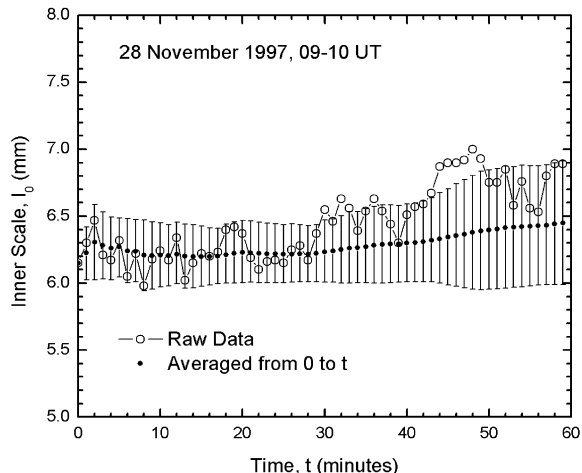
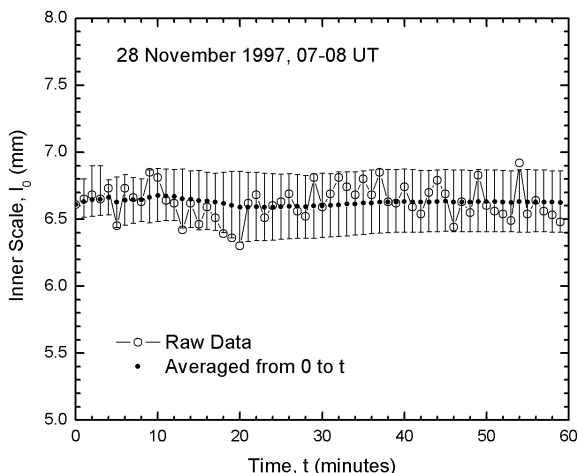
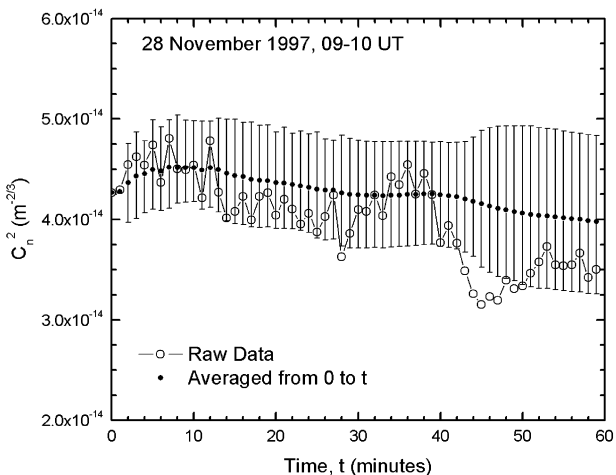
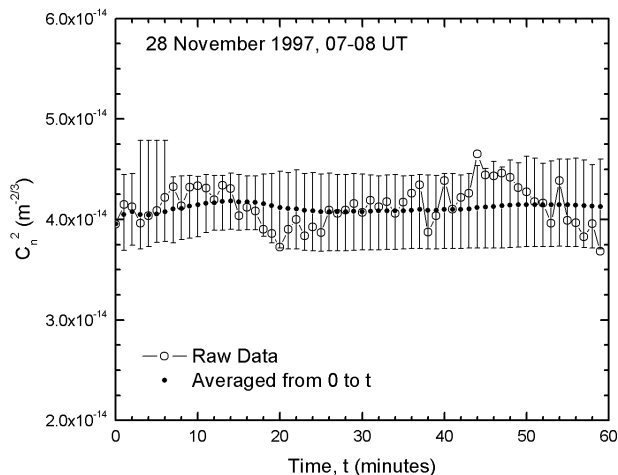


FIG. 5. Hour-long time series of the 1-min-averaged values of (top)  $C_n^2$  and (bottom)  $l_0$  and averages of these computed from (14) from time zero until the plotted time,  $t$ . The errors bars show 90% confidence intervals on the population based on a beta distribution computed from the average and standard deviation at time  $t$  [i.e., from (14) and (15)].

FIG. 6. As in Fig. 5, but 2 h later.

30–60 min to match the averaging represented in the Monin–Obukhov similarity functions would not have changed the  $C_n^2$  and  $l_0$  averages significantly.

To confirm this conclusion, we estimated  $u_*$  and  $H_s$  from these time series using (5)–(7) and the similarity functions  $g(\zeta)$  and  $\phi_s(\zeta)$  given in the appendix. The averages of the first 10 min of  $C_n^2$  and  $l_0$  values give  $u_*$  and  $H_s$  values of  $0.0745 \text{ m s}^{-1}$  and  $-6.68 \text{ W m}^{-2}$ , respectively, while the  $C_n^2$  and  $l_0$  averages for the entire 60-min series yield values of  $0.0754 \text{ m s}^{-1}$  and  $-6.78 \text{ W m}^{-2}$ . That is, the differences here between fluxes based on 60-min averages and averages of only the first 10 min of the series are about 1% for both  $u_*$  and  $H_s$ . In fact, the  $u_*$  and  $H_s$  values computed from these 60-min series are within about 3% of the  $u_*$  and  $H_s$  values computed from the hourly averages of  $C_n^2$  and

$l_0$ . Again, these results support the premise that path-averaging instruments provide accurate estimates of the surface fluxes quickly.

The histograms in Fig. 3 and the time series in Fig. 6, however, present a different situation just 2 h later. During this hour,  $C_n^2$  has a downward trend while  $l_0$  has an upward trend. Both series also show shorter periods of nonstationarity. As a result, the 90% confidence interval for the  $C_n^2$  population calculated from 10 min of data brackets fewer than one-half of the subsequent minute averages and does not even include the  $C_n^2$  average at the end of the hour. Likewise, the 90% confidence interval for the  $l_0$  population obtained from 10 min of averaging brackets fewer than one-half of the subsequent minute averages of  $l_0$  and barely includes the  $l_0$  average at the end of the hour. In other words, for the data in Figs. 3 and 6, 10 min of averaging does not faithfully predict the variability of the  $C_n^2$  and  $l_0$  values that occur during this hour.

This example thus refutes the hypothesis that short-term averages of  $C_n^2$  and  $l_0$  can, in general, yield mean-

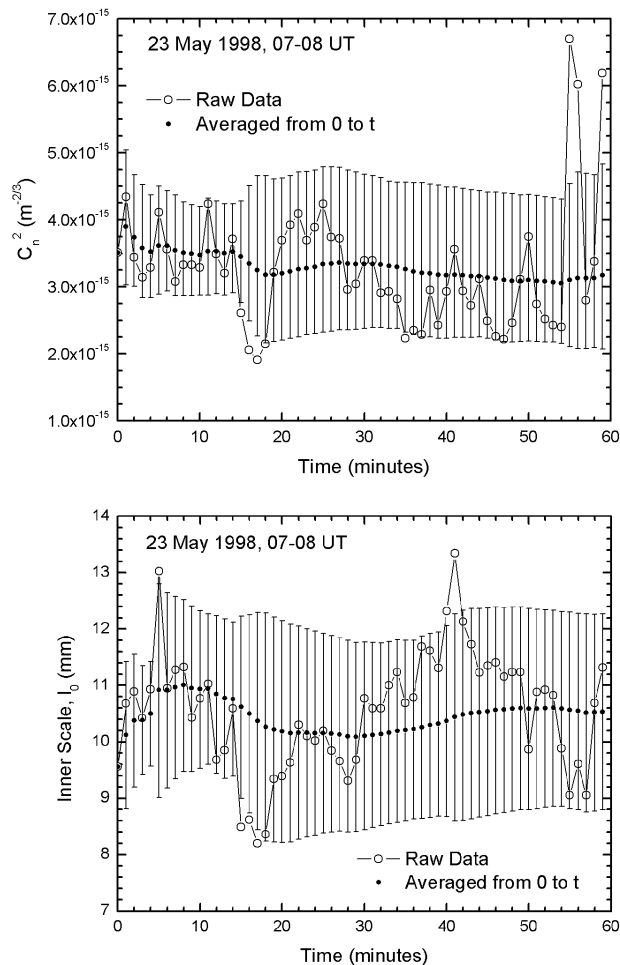


FIG. 7. As in Fig. 5, but in May 1998.

ingful estimates of the surface momentum and sensible heat fluxes. Here, because of the nonstationarity, it is not obvious that short-term  $C_n^2$  and  $l_0$  averages can be meaningfully convolved with functions based on 30–60 min of averaging. In essence, nonstationarity confounds path-averaging sensors just as it confounds point sensors.

To demonstrate, we again compare  $u_*$  and  $H_s$  values computed from the first 10 min, of these  $C_n^2$  and  $l_0$  series and from the entire series. For the first 10 min,  $C_n^2$  and  $l_0$  averages yield  $u_*$  and  $H_s$  values of  $0.0844 \text{ m s}^{-1}$  and  $-8.18 \text{ W m}^{-2}$ , respectively, while the 60-min averages yield values of  $0.0795 \text{ m s}^{-1}$  and  $-7.18 \text{ W m}^{-2}$ . These  $u_*$  values differ by 6.1%, while the  $H_s$  values differ by 13.9%. The fourth 10-min block in these series produces worse results; the  $u_*$  and  $H_s$  values based on these 10-min averages differ from values based on the 60-min averages by 7.8% and 15.6%, respectively.

While these differences in the  $H_s$  estimate, in particular, are not large in magnitude, the percentage differences are significant. In midlatitudes, over land, these

$H_s$  can be  $200\text{--}300 \text{ W m}^{-2}$ , for example, a 15% uncertainty in  $H_s$  amounts to  $30\text{--}45 \text{ W m}^{-2}$ . Such an uncertainty is much too large if we have intentions, for instance, to ever use scintillation to improve climatological estimates of the surface heat budget, where an accuracy of  $5\text{--}10 \text{ W m}^{-2}$  is essential (e.g., Mitchell 1989; Kiehl and Trenberth 1997).

Figure 7 shows another hour of  $C_n^2$  and  $l_0$  values from May 1998 to emphasize these points. (The corresponding histograms are in Fig. 4.) In contrast to Fig. 6, the  $C_n^2$  and  $l_0$  time series here do not have trends but do display a lot of variability. As a result, although the confidence interval on the  $C_n^2$  population at 10 min brackets all subsequent  $C_n^2$  averages, it brackets only about one-half of the subsequent 1-min averages. The situation is not quite as bad for the  $l_0$  series, mainly because variability early in the series leads to a large 90% confidence interval for the population after 10 min of averaging. Still, 20% of the subsequent minute-averaged  $l_0$  values are outside this 90% confidence interval, and the confidence interval for the population after 1 h of averaging is 25% larger than the confidence interval at 10 min.

Hence, again, 10 min of scintillometer data did not provide a very accurate picture of the  $C_n^2$  and  $l_0$  populations we encountered during this hour. Therefore, it does not seem prudent to use, say, the 10-min-averaged  $C_n^2$  and  $l_0$  values from these series in inertial–dissipation estimates of the surface fluxes. The nonstationarity leads to confidence intervals for the  $C_n^2$  and  $l_0$  populations with widths that are significant fractions of the respective mean values: about 35% for  $C_n^2$  and about 17% for  $l_0$  after 1 h of averaging. We would not be making very reliable estimates of the surface fluxes.

To confirm this conclusion, we again compare calculations of  $u_*$  and  $H_s$  based on the first 10 min of these  $C_n^2$  and  $l_0$  times series and on the entire 60-min series. The first 10 min yields  $u_*$  and  $H_s$  values of  $0.0451 \text{ m s}^{-1}$  and  $-1.32 \text{ W m}^{-2}$ , respectively, while the 60-min  $C_n^2$  and  $l_0$  averages yield values of  $0.0488 \text{ m s}^{-1}$  and  $-1.42 \text{ W m}^{-2}$ . These values differ by 7%–8%. Averages of  $C_n^2$  and  $l_0$  from the second 10-min block in these series, however, yield  $u_*$  and  $H_s$  values that differ from the 60-min averages by 22% and 24%, respectively. These are large excursions from the long-term means despite the fact that these data from 10–19 min were also used to compute the 60-min averages.

The idea that path-averaging instruments can yield meaningful estimates of turbulent surface fluxes in a fraction of the time that point measurements can springs from the hope that the path-averaging would quickly sample enough turbulent eddies to minimize the effects of nonstationarity. As Figs. 6 and 7 demonstrate, for propagation paths of 300–350 m at least, this does not happen in general. Nonstationarity is still a problem for path-averaging instruments.

## 6. Quantifying the nonstationarity

Because nonstationarity presents sampling problems for path-averaging sensors as well as for point sensors,

TABLE 1. Calculations of the nonstationarity ratio from (16) for the raw  $C_n^2$  and  $l_0$  series shown in Figs. 5–7 for two choices of  $I$  and  $J$ . “Average” denotes the 1-h average, “crossings” counts the number of times the series crosses this average, and “59/crossings” (or  $M/C$ ) is another measure of nonstationarity explained in the text.

|                        | 28 Nov 1997<br>0700–0800<br>UTC<br>(Fig. 5) | 28 Nov 1997<br>0900–1000<br>UTC<br>(Fig. 6) | 23 May 1998<br>0700–0800<br>UTC<br>(Fig. 7) |
|------------------------|---|---|---|
|                        | $C_n^2$                                     |   |   |
| Average ( $m^{-2/3}$ ) | $4.14 \times 10^{-14}$                      | $4.01 \times 10^{-14}$                      | $3.27 \times 10^{-15}$                      |
| NR                     |   |   |   |
| $I = 6, J = 10$        | 2.75  | 7.05  | 2.23  |
| $I = 10, J = 6$        | 2.97  | 5.27  | 2.23  |
| Crossings              | 20  | 9   | 18  |
| 59/crossings           | 2.95  | 6.55  | 3.28  |
|                        | $l_0$                                       |   |   |
| Average (mm)           | 6.62  | 6.45  | 10.54                                       |
| NR                     |   |   |   |
| $I = 6, J = 10$        | 1.63  | 6.54  | 3.77  |
| $I = 10, J = 6$        | 1.68  | 5.36  | 3.35  |
| Crossings              | 22  | 7   | 13  |
| 59/crossings           | 2.68  | 8.43  | 4.54  |

we use our scintillometer data to study ways to quantify this nonstationarity. Mahrt (1998) defines a “nonstationarity ratio” just for this purpose. We adapt his method to our data.

To use Mahrt’s (1998) method, we divide our 60-sample (i.e., 1 h) time series into  $I$  records of  $J$  samples each, where  $I \times J = 60$ . Mahrt first defines the “within record” standard deviation that then leads to an estimate of the random error RE in the series. He next defines the “between record” standard deviation  $s_{\text{btw}}$ . His nonstationarity ratio is then

$$\text{NR} = s_{\text{btw}}/\text{RE}. \tag{16}$$

Conceptually,  $s_{\text{btw}}$  is large when nonstationarity produces long segments of the series that remain above or below the series mean, as in both the  $C_n^2$  and  $l_0$  series in Fig. 6. On the other hand, RE is large and NR tends to be smaller when the time series has a large amount of random variability, as in the  $C_n^2$  plot in Fig. 7. Thus, Mahrt’s (1998) nonstationarity ratio compares the effects of coherent behavior with the inherent variability in the time series. According to Mahrt, “for stationary conditions, NR is approximately unity.” Nonstationarity ratio values significantly larger than 1 indicate nonstationarity.

We have calculated NR twice each for the raw 60-min  $C_n^2$  and  $l_0$  time series plotted in Figs. 5–7 to see if this ratio can complement our analysis in the previous section. In one case,  $I = 6$  and  $J = 10$ ; in the other case,  $I = 10$  and  $J = 6$ . Table 1 summarizes the results.

The first thing we notice in the table is that the NR values calculated for the two  $I$ – $J$  pairs are not necessarily the same. For the  $C_n^2$  and  $l_0$  traces in Figs. 5 and 7, the respective NRs for the two  $I$ – $J$  pairs are similar, if not identical. For Fig. 6, however, the NRs for  $C_n^2$ ,

7.05 and 5.27, and for  $l_0$ , 6.54 and 5.36, each differ by over 20%. Mahrt (1998) does not suggest any guidelines for choosing  $I$  or  $J$ , but, from the basis for his method, we believe that the samples per record,  $J$ , should represent a period that is typical of the large-scale variability in the signal. The  $C_n^2$  and  $l_0$  traces in Fig. 6 seem to have large-scale coherence for periods longer than 6 min. As a result, the  $J = 10$  and  $J = 6$  calculations yield significantly different results for these series.

On the other hand, the nonstationarity ratios listed in Table 1 both confirm some of our previous conclusions that we based on confidence intervals and contrast with them. For example, the  $C_n^2$  and  $l_0$  traces in Fig. 5 are well behaved, and we had concluded that short-term averages from these series would be useful for estimating fluxes. Likewise, the NR values for these series for both  $I$ – $J$  pairs are consistent and are two of the three smallest collections in the table. In particular, the NRs for the  $l_0$  series, 1.6–1.7, are near 1, the value Mahrt (1998) associates with a stationary time series.

The nonstationarity ratios also corroborate our evaluation of the  $C_n^2$  and  $l_0$  series in Fig. 6. These both had unacceptable short-term behavior, largely because of their trends, and the NRs for these are the four largest values in the table. Evidently, if a series is stationary, the choice of  $I$  and  $J$  is not too crucial: both  $I$ – $J$  pairs yield comparable NR values for both the  $C_n^2$  and  $l_0$  traces in Fig. 5. When a series is nonstationary, however, as is Fig. 6, different choices for  $I$  and  $J$  can yield markedly different values of NR. These NR values, nevertheless, are large and do suggest what they should—that the series is nonstationary.

Last, the nonstationarity ratios for the  $C_n^2$  and  $l_0$  series in Fig. 7 suggest conclusions that contrast with our earlier discussion of these series. We had also judged these two series unreliable for producing short-term averages because of their large variability. The NRs of the  $C_n^2$  series in Fig. 7, however, both 2.23, are smaller than the NR of the supposedly “good”  $C_n^2$  series in Fig. 5. The NR values for the  $l_0$  series, 3.77 and 3.35, are larger than the NRs for the  $C_n^2$  series, although we had earlier concluded that the  $l_0$  series in Fig. 7 was “better” for averaging than the  $C_n^2$  series on the basis of our uncertainty analysis. These two discrepancies raise questions about what nonstationarity means in general and what Mahrt’s (1998) nonstationarity ratio quantifies in particular.

We see that NR, through its linear dependence on the between-record variability  $s_{\text{btw}}$  in (16) tends to be large if coherent sections of the record are above or below the mean. On the other hand, because of its inverse dependence on the random error, RE, NR tends to be small if the time series has large-amplitude random variability. The  $C_n^2$  trace in Fig. 7 has such large-amplitude variability (i.e., large RE), but the events are not necessarily coherent (i.e., small  $s_{\text{btw}}$ ). As a result, the NR for this series is relatively small despite error bars that increase with time. The  $l_0$  trace in Fig. 7, in contrast,

has large-amplitude variability (i.e., large RE), but that variability is more coherent. There are, essentially, four segments in the time series: two above and two below the mean. Thus,  $s_{\text{btw}}$  is also large, and this combination yields midrange NRs that are larger than the NRs for the  $C_n^2$  series.

In summary, according to Mahrt's (1998) definition of nonstationarity, as formalized in his nonstationarity ratio NR, two effects contribute most to nonstationarity: a trend, and large, coherent excursions from the mean. By "large" here, we mean events that span a significant fraction of the time series, say 10% of it.

Again according to Mahrt (1998), large-amplitude, random variability is the opposite of nonstationarity: this variability actually reduces his nonstationarity ratio. In essence, if a series is highly variable, coherent excursions from the mean should not be surprising and, thus, should not be judged as nonstationarity. In our uncertainty-based analysis, however, such highly variable series lead to wide confidence intervals and, in turn, to uncertain estimates of the surface fluxes. In other words, nonstationarity (at least as defined by Mahrt) is not the sole cause of uncertain flux estimates: random variability also leads to uncertainty.

These insights into Mahrt's (1998) nonstationarity ratio led us to realize that, generally, a stationary time series exhibits many zero crossings, while a nonstationary series has long segments above or below zero. (Here, zero crossings refer to a series with the mean removed.) Table 1 also lists the number of zero crossings for the raw  $C_n^2$  and  $l_0$  series in Figs. 5–7, where that count includes both up-going and down-going zero crossings. These counts mirror our analysis based on NR. The  $C_n^2$  and  $l_0$  series in Fig. 5 have many crossings and small NR, the series in Fig. 6 have few crossings and large NR, and the series in Fig. 7 have intermediate numbers of crossings and, generally, intermediate NR.

A series of 60 samples can cross zero at most 59 times and must cross zero at least once. Denote the number of crossings as  $C$  and this maximum number of crossings as  $M$ . Clearly,  $1 \leq M/C \leq M$ . Mahrt's (1998) NR, in contrast, is not necessarily always greater than or equal to 1; we have created artificial series with NR less than 1 (for example, a 60-point square wave of amplitude 1 and wavelength 12). It seems useful to have a nonstationarity metric with obvious lower and upper limits. In counting zero crossings,  $M/C = 1$  would mean that each consecutive point switches from above to below the mean or vice versa. Of course, such a series is improbable; the point is that  $M/C$  has an obvious lower limit, and a value near this limit is a good indicator that the series is stationary. In contrast,  $M/C = M$  would mean the series crosses zero only once and, thus, has a trend.

The  $M/C$  values in Table 1 (i.e., "59/Crossings") are similar in both magnitude and tendency to the corresponding NRs;  $M/C$ , therefore, seems to be a nonstationarity metric that is as good as NR. Counting zero

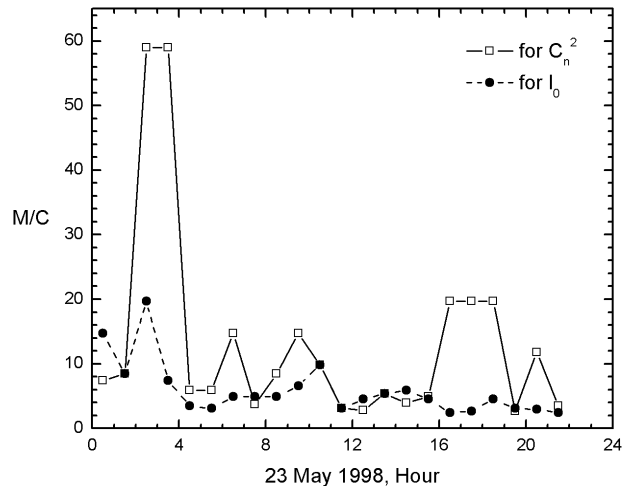


FIG. 8. The nonstationarity metric  $M/C$  for hourly segments of the  $C_n^2$  and  $l_0$  time series in Fig. 1, where  $M$  is always 59 ( $=60 - 1$ ) and  $C$  counts the zero crossings during the hour. Values are plotted at the midpoint of the hour. Because during the last 2 h the series in Fig. 1 had gaps, we calculated no  $M/C$  values for these hours.

crossings is also much easier than making the calculations necessary to evaluate NR. Another benefit is that counting zero crossings obviates the need to make arbitrary choices of  $I$  and  $J$ .

To develop a better sense of what this zero-crossing metric tells us about a time series, we computed  $M/C$  for hourly intervals of the  $C_n^2$  and  $l_0$  time series in Fig. 1. Figure 8 shows the results.

The first thing this figure suggests is that, on this day,  $C_n^2$  was much more nonstationary than  $l_0$  was. In fact, between 0200 and 0400 UTC, when  $C_n^2$  climbed steadily through two orders of magnitude (see Fig. 1), its  $M/C$  value was at its maximum, 59. That is,  $C_n^2$  had only one zero crossing each hour. During the steady decline from 1600 to 1900 UTC in Fig. 1,  $C_n^2$  also had large  $M/C$  values, almost 20 (i.e., three zero crossings during each hour).

The largest  $M/C$  value for the  $l_0$  record in Fig. 1 also occurs for 0200–0300 UTC, when  $l_0$  is climbing out of its local minimum. The  $l_0$  record also has large  $M/C$  values for 0000–0100 UTC and 1000–1100 UTC, when  $l_0$  undergoes some large, coherent excursions. We conclude from Fig. 8 that  $M/C$  is a good indicator of a trend in a time series and of coherent excursions on either side of the mean.

Last, Fig. 8 suggests that  $C_n^2$  and  $l_0$  were both stationary during the 5-h period 1100–1600 UTC. Here, the  $M/C$  values for both  $C_n^2$  and  $l_0$  are between 2 and 6. Likewise, the  $C_n^2$  and  $l_0$  traces in Fig. 1 show fairly constant levels here and more modest fluctuations than in the rest of the records. We thus recommend considering a time series to be stationary if  $M/C$  is less than 6.

## 7. Conclusions

Our SHEBA scintillometer data confirm Andreas's (1989a) conclusion that a beta distribution with lower

and upper limits corresponding to  $10^{-18}$  and  $10^{-12} \text{ m}^{-2/3}$  reliably models the distribution of Arctic near-surface  $C_n^2$  values. We are, evidently, the first to report that a beta distribution with lower and upper limits of 0 and 20 mm is also useful for representing values of the inner scale of turbulence,  $l_0$ .

Using this knowledge of the sampling distributions for  $C_n^2$  and  $l_0$ , we have investigated whether short-term averages of path-averaged  $C_n^2$  and  $l_0$  values can yield reliable estimates of the surface stress and the surface sensible heat flux through an inertial–dissipation calculation. The answer turns on the fact that the similarity functions used in the inertial–dissipation calculations derive from point measurements based on averages of 30–60 min. The cautious approach is to convolve short-term averages of  $C_n^2$  and  $l_0$  (i.e., on the order of minutes) with these similarity functions only if short records of  $C_n^2$  and  $l_0$  fairly represent the behavior of time series over 30–60 min.

Three typical hour-long time series of  $C_n^2$  and  $l_0$  measurements from SHEBA imply that path averaging confers no general benefits when the objective is to shorten the averaging time for flux sampling. Short-term series simply do not always bracket the behavior of 30–60-min series. If the  $C_n^2$  and  $l_0$  time series, however, are stationary over, say, hourly intervals, the fluxes of heat and momentum computed over 10-min subrecords can be statistically reliable. That is, for stationary series, it is safe to convolve short-term  $C_n^2$  and  $l_0$  averages with similarity functions derived from longer averaging.

But nonstationarity leads to uncertain flux measurements with path-averaging instruments just as it does for point measurements, at least for averaging paths of 300–350 m. On the basis of our three examples and the averaging estimates we reviewed in section 3, we expect estimates of  $\tau$  and  $H_s$  to easily vary by 20% or more between adjacent 10-min subrecords. This is the random error resulting from variability in  $C_n^2$  and  $l_0$ . Estimates of  $\tau$  and  $H_s$  could also suffer from bias errors caused by using similarity functions unproven for short-term averaging. Admittedly though, in some applications, both errors may be tolerable.

In our view, the best way to ensure reliable short-term flux estimates from scintillometer data is to first validate the Monin–Obukhov similarity functions from measurements of short-term averages. That is, make point measurements of, say, 10-min averages of the vertical wind speed and temperature gradients and the fluxes  $\overline{uw}$  and  $\overline{wt}$  and see how well these data fit known functions for  $\phi_\epsilon(\zeta)$  and  $g(\zeta)$ . Though the computed functions will be quite scattered, perhaps we will see the same  $\phi_\epsilon(\zeta)$  and  $g(\zeta)$  functions emerging that longer averaging has yielded. If so, the experiment establishes the validity of Monin–Obukhov similarity for short-term averages and puts scintillometer flux analysis on firm theoretical and experimental footing. To our knowledge,

however, this experiment has never been done, and there are no guarantees that it will succeed.

Because nonstationarity turned out to be one key for deciding whether a flux estimate was reliable, we evaluated two metrics for quantifying nonstationarity. Mahrt’s (1998) nonstationarity ratio tended to corroborate our analysis of the utility of  $C_n^2$  and  $l_0$  for estimating fluxes that we based on assigning confidence intervals. That is, acceptable  $C_n^2$  and  $l_0$  series generally had small values of NR, while unacceptable series had larger NRs. We did identify some examples that went against intuition, however. These series had large-amplitude, random variability and, thus, produced averages with large uncertainty; still, their NRs were fairly small. One manifestation of nonstationarity is, thus, extended segments of the series either above or below the mean. High random variability, on the other hand, is the opposite of nonstationarity, but still degrades flux estimates.

In light of these insights, we realized that the number of zero crossings,  $C$ , in a series is another useful measure of nonstationarity. A benefit of this metric is that a series of  $M + 1$  data points can display no more than  $M$  zero crossings and must have at least one zero crossing. Consequently,  $M/C$  assumes values from 1 to  $M$ . When it is 1, consecutive points in the series just switch back and forth between positive and negative—an obviously stationary series. When it is  $M$ , the series crosses zero only once because of a strong trend. Last, because in our six examples the  $M/C$  values are remarkably near the corresponding NRs calculated with Mahrt’s (1998) method,  $M/C$  is another simple measure of nonstationarity.

*Acknowledgments.* We thank Kerry Claffey, Dave Costa, Janet Intrieri, Jeff Otten, and Dominique Ruffieux for important contributions to our experimental program. We also thank George Treviño, Larry Mahrt, and three anonymous reviewers for comments that helped us to improve the manuscript. The U.S. Department of the Army supported the first author in this work through Project 4A1611AT24. The U.S. National Science Foundation also supported this work with awards to the Army’s Cold Regions Research and Engineering Laboratory (OPP-97-02025 and OPP-00-84190), NOAA’s Environmental Technology Laboratory (OPP-97-01766 and OPP-00-84323), and the Naval Postgraduate School (OPP-97-01390 and OPP-00-84279). We dedicate this paper to the memory of Marvin L. Wesely. At the time of his death, he was the editor of the *Journal of Applied Meteorology* in charge of its review. In addition, his early work on scintillation paved the way for our research.

## APPENDIX

### The Similarity Functions $g(\zeta)$ and $\phi_\epsilon(\zeta)$

For  $\phi_\epsilon$  in (7), we use

$$\phi_\epsilon(\zeta) = [1 + 0.46(-\zeta)^{2/3}]^{3/2} \quad (\text{A1})$$

in unstable stratification ( $\zeta \leq 0$ ) and

$$\phi_\varepsilon(\zeta) = [1 + 2.3\zeta^{3/5}]^{3/2} \quad (\text{A2})$$

in stable stratification ( $\zeta \geq 0$ ). These functions are from Wyngaard and Coté (1971), but Andreas (1988b) modified their original coefficients to reflect a von Kármán constant of 0.40 rather than the 0.35 that they assumed. Here also,

$$\zeta = \frac{z}{L} = \frac{kz\hat{g}}{T_v} \frac{t_*}{u_*^2}, \quad (\text{A3})$$

where  $L$  is the Obukhov length,  $\hat{g}$  is the acceleration of gravity, and  $T_v$  is the average virtual temperature.

Stable stratification is a special concern of ours in this SHEBA dataset. Andreas (2002) discusses the Monin–Obukhov similarity functions for stable stratification and recommends Holtslag and De Bruin's (1988) formulation for the dimensionless temperature profile function,

$$\phi_h(\zeta) = 1 + 0.7\zeta + 0.75\zeta(6 - 0.35\zeta) \exp(-0.35\zeta). \quad (\text{A4})$$

This has the best properties among the available  $\phi_h$  functions in very stable stratification. We incorporate the desirable properties of this function into our  $g(\zeta)$  equation, (6), by using the expression for  $g(\zeta)$  that Andreas (1988b) derives from the scalar variance budget. That is,

$$g(\zeta) = \frac{5.92\phi_h(\zeta)}{\phi_\varepsilon^{1/3}(\zeta)}, \quad (\text{A5})$$

where, for stable stratification, we use (A2) for  $\phi_\varepsilon$  and (A4) for  $\phi_h$ .

In unstable stratification, we use (Edson and Fairall 1998)

$$g(\zeta) = 5.92(1 - 8\zeta)^{-2/3} \quad (\text{A6})$$

because it matches (A5) best at  $\zeta = 0$ .

#### REFERENCES

- Andreas, E. L., 1987: On the Kolmogorov constants for the temperature-humidity cospectrum and the refractive index spectrum. *J. Atmos. Sci.*, **44**, 2399–2406.
- , 1988a: Estimating averaging times for point and path-averaged measurements of turbulence spectra. *J. Appl. Meteor.*, **27**, 295–304.
- , 1988b: Estimating  $C_n^2$  over snow and sea ice from meteorological data. *J. Opt. Soc. Amer.*, **5A**, 481–495.
- , 1989a: The refractive index structure parameter,  $C_n^2$ , for a year over the frozen Beaufort Sea. *Radio Sci.*, **24**, 667–679.
- , 1989b: Two-wavelength method of measuring path-averaged turbulent surface heat fluxes. *J. Atmos. Oceanic Technol.*, **6**, 280–292.
- , 1990: *Selected Papers on Turbulence in a Refractive Medium*. Society of Photo-Optical Instrumentation Engineers Milestone Series, Vol. 25, SPIE, 693 pp.
- , 1992: Uncertainty in a path-averaged measurement of the friction velocity  $u_*$ . *J. Appl. Meteor.*, **31**, 1312–1321.
- , 2002: Parameterizing scalar transfer over snow and ice: A review. *J. Hydrometeorol.*, **3**, 417–432.
- , and B. A. Cash, 1996: A new formulation for the Bowen ratio over saturated surfaces. *J. Appl. Meteor.*, **35**, 1279–1289.
- , C. W. Fairall, P. S. Guest, and P. O. G. Persson, 1999: An overview of the SHEBA atmospheric surface flux program. Preprints, *Fifth Conf. on Polar Meteorology and Oceanography*, Dallas, TX, Amer. Meteor. Soc., 411–416.
- , —, P. O. G. Persson, and P. S. Guest, 2000: Probability distributions for scintillometer-derived values of the inner scale and the refractive index structure parameter and their implications for averaging. Preprints, *14th Symp. on Boundary Layers and Turbulence*, Aspen, CO, Amer. Meteor. Soc., 19–22.
- Arya, S. P., 1988: *Introduction to Micrometeorology*. Academic Press, 307 pp.
- Ben-Yosef, N., and E. Goldner, 1988: Splitting-source model for the statistics of irradiance scintillations. *J. Opt. Soc. Amer.*, **5A**, 126–131.
- Businger, J. A., J. C. Wyngaard, Y. Izumi, and E. F. Bradley, 1971: Flux-profile relationships in the atmospheric surface layer. *J. Atmos. Sci.*, **28**, 181–189.
- Chernov, L. A., 1967: *Wave Propagation in a Random Medium*. Dover, 168 pp.
- De Bruin, H. A. R., B. J. J. M. van den Hurk, and W. Kohsiek, 1995: The scintillation method tested over a dry vineyard area. *Bound.-Layer Meteorol.*, **76**, 25–40.
- , W. M. L. Meijninger, A.-S. Smedman, and M. Magnusson, 2002: Displaced-beam small aperture scintillometer test. Part I: The WINTEX data-set. *Bound.-Layer Meteorol.*, **105**, 129–148.
- Dyer, A. J., and E. F. Bradley, 1982: An alternative analysis of flux-gradient relationships at the 1976 ITCE. *Bound.-Layer Meteorol.*, **22**, 3–19.
- Edson, J. B., and C. W. Fairall, 1998: Similarity relationships in the marine atmospheric surface layer for terms in the TKE and scalar variance budgets. *J. Atmos. Sci.*, **55**, 2311–2328.
- Fairall, C. W., and S. E. Larsen, 1986: Inertial-dissipation methods and turbulent fluxes at the air-ocean interface. *Bound.-Layer Meteorol.*, **34**, 287–301.
- Frederickson, P. A., K. L. Davidson, C. R. Zeisse, and C. S. Bendall, 2000: Estimating the refractive index structure parameter ( $C_n^2$ ) over the ocean using bulk methods. *J. Appl. Meteorol.*, **39**, 1770–1783.
- Frehlich, R. G., 1988: Estimation of the parameters of the atmospheric turbulence spectrum using measurements of the spatial intensity covariance. *Appl. Opt.*, **27**, 2194–2198.
- , 1992: Laser scintillation measurements of the temperature spectrum in the atmospheric surface layer. *J. Atmos. Sci.*, **49**, 1494–1509.
- Gray, D. A., and A. T. Waterman Jr., 1970: Measurement of fine-scale atmospheric structure using an optical propagation technique. *J. Geophys. Res.*, **75**, 1077–1083.
- Green, A. E., K. J. McAneney, and M. S. Astill, 1994: Surface-layer scintillation measurements of daytime sensible heat and momentum fluxes. *Bound.-Layer Meteorol.*, **68**, 357–373.
- Gurvich, A. S., N. S. Time, L. S. Turovtseva, and V. F. Turchin, 1974: Reconstruction of the temperature fluctuation spectrum of the atmosphere from optical measurements. *Izv., Atmos. Oceanic Phys.*, **10**, 292–297.
- Harr, M. E., 1987: *Reliability-Based Design in Civil Engineering*. McGraw-Hill, 543 pp.
- Hartogensis, O. K., H. A. R. De Bruin, and B. J. H. Van de Wiel, 2002: Displaced-beam small aperture scintillometer test. Part II: CASES-99 stable boundary-layer experiment. *Bound.-Layer Meteorol.*, **105**, 149–176.
- Haugen, D. A., J. C. Kaimal, and E. F. Bradley, 1971: An experimental study of Reynolds stress and heat flux in the atmospheric surface layer. *Quart. J. Roy. Meteor. Soc.*, **97**, 168–180.
- Hill, R. J., 1997: Algorithms for obtaining atmospheric surface-layer fluxes from scintillation measurements. *J. Atmos. Oceanic Technol.*, **14**, 456–467.
- , and S. F. Clifford, 1978: Modified spectrum of atmospheric

- temperature fluctuations and its application to optical propagation. *J. Opt. Soc. Amer.*, **68**, 892–899.
- , and R. G. Frehlich, 1997: Probability distribution of irradiance for the onset of strong scintillation. *J. Opt. Soc. Amer.*, **14A**, 1530–1540.
- , R. A. Bohlander, S. F. Clifford, R. W. McMillan, J. T. Priestley, and W. P. Schoenfeld, 1988: Turbulence-induced millimeter-wave scintillation compared with micrometeorological measurements. *IEEE Trans. Geosci. Remote Sens.*, **26**, 330–342.
- , G. R. Ochs, and J. J. Wilson, 1992a: Measuring surface-layer fluxes of heat and momentum using optical scintillation. *Bound.-Layer Meteor.*, **58**, 391–408.
- , —, and —, 1992b: Surface-layer fluxes measured using the  $C_2^2$ -profile method. *J. Atmos. Oceanic Technol.*, **9**, 526–537.
- Högström, U., 1988: Non-dimensional wind and temperature profiles in the atmospheric surface layer: A re-evaluation. *Bound.-Layer Meteor.*, **42**, 55–78.
- Holtstag, A. A. M., and H. A. R. De Bruin, 1988: Applied modeling of the nighttime surface energy balance over land. *J. Appl. Meteor.*, **27**, 689–704.
- Kiehl, J. T., and K. E. Trenberth, 1997: Earth's annual global mean energy budget. *Bull. Amer. Meteor. Soc.*, **78**, 197–208.
- Kohsiek, W., and M. H. A. J. Herben, 1983: Evaporation derived from optical and radio-wave scintillation. *Appl. Opt.*, **22**, 2566–2570.
- Lenschow, D. H., J. Mann, and L. Kristensen, 1994: How long is long enough when measuring fluxes and other turbulence statistics? *J. Atmos. Oceanic Technol.*, **11**, 661–673.
- Lumley, J. L., and H. A. Panofsky, 1964: *The Structure of Atmospheric Turbulence*. Interscience, 239 pp.
- Mahrt, L., 1998: Flux sampling errors for aircraft and towers. *J. Atmos. Oceanic Technol.*, **15**, 416–429.
- Mitchell, J. F. B., 1989: The “greenhouse” effect and climate change. *Rev. Geophys.*, **27**, 115–139.
- Nieveen, J. P., and A. E. Green, 1999: Measuring sensible heat flux density over pasture using the  $C_2^2$ -profile method. *Bound.-Layer Meteor.*, **91**, 23–35.
- Oncley, S. P., C. A. Friehe, J. C. Larue, J. A. Businger, E. C. Itsweire, and S. S. Chang, 1996: Surface-layer fluxes, profiles, and turbulence measurements over uniform terrain under near-neutral conditions. *J. Atmos. Sci.*, **53**, 1029–1044.
- Persson, P. O. G., C. W. Fairall, E. L. Andreas, P. S. Guest, and D. K. Perovich, 2002: Measurements near the Atmospheric Surface Flux Group tower at SHEBA: Near-surface conditions and surface energy budget. *J. Geophys. Res.*, **107**, 8045, doi:10.1029/2000JC000705.
- Sreenivasan, K. R., A. J. Chambers, and R. A. Antonia, 1978: Accuracy of moments of velocity and scalar fluctuations in the atmospheric surface layer. *Bound.-Layer Meteor.*, **14**, 341–359.
- Strohbeh, J. W., 1970: The feasibility of laser experiments for measuring the permittivity spectrum of the turbulent atmosphere. *J. Geophys. Res.*, **75**, 1067–1076.
- Tatarskii, V. I., 1961: *Wave Propagation in a Turbulent Medium*. Dover, 285 pp.
- , 1971: *The Effects of the Turbulent Atmosphere on Wave Propagation*. Israel Program for Scientific Translations, 472 pp.
- Thiermann, V., 1992: A displaced-beam scintillometer for line-averaged measurements of surface layer turbulence. Preprints, *10th Symp. on Turbulence and Diffusion*, Portland, OR, Amer. Meteor. Soc., 244–247.
- , and H. Grassl, 1992: The measurement of turbulent surface-layer fluxes by use of bichromatic scintillation. *Bound.-Layer Meteor.*, **58**, 367–389.
- Uttal, T., and Coauthors, 2002: Surface Heat Budget of the Arctic Ocean. *Bull. Amer. Meteor. Soc.*, **83**, 255–275.
- Wesely, M. L., 1976: The combined effect of temperature and humidity fluctuations on refractive index. *J. Appl. Meteor.*, **15**, 43–49.
- , and E. C. Alcaez, 1973: Diurnal cycles of the refractive index structure function coefficient. *J. Geophys. Res.*, **78**, 6224–6232.
- Wyngaard, J. C., 1973: On surface-layer turbulence. *Workshop on Micrometeorology*, D. A. Haugen, Ed., Amer. Meteor. Soc., 101–149.
- , and O. R. Coté, 1971: The budgets of turbulent kinetic energy and temperature variance in the atmospheric surface layer. *J. Atmos. Sci.*, **28**, 190–201.
- , and S. F. Clifford, 1978: Estimating momentum, heat and moisture fluxes from structure parameters. *J. Atmos. Sci.*, **35**, 1204–1211.

